Supporting Information

Donald et al. 10.1073/pnas.1019668108

SI Text

Peptide Synthesis, cleavage and purification. The wild-type sequence for parainfluenza virus 5 (PIV5) fusion peptide (FP) is FAGV VIGLAALGVATAAQVTAAVALVKANE. The only glutamine, residue 120 (using the numbering of the fusion protein before cleavage), was mutated into alanine for the mutant Q120A. One tryptophan was added to the C-terminus of both the wild-type FP and the mutant Q120A using a flexible $(Gly)_3$ linker in order to provide absorbance at 280 nm for concentration measurements. The sequence used for the C-terminal membrane segment transmembrane (C-term-TM) peptide is VLSIIAIALGSLGLILIIILL-SVVVWK and contains a tryptophan for concentration measurements and a conservative Cys to Ala mutation at 492 to avoid nonbiological disulfide crosslinking.

Peptide synthesis, cleavage, and purification were conducted as previously described (1). A 0.1 mmole scale synthesis was manually conducted on RINK amide resin (Novabiochem) by N-9-fluorenylmethyloxycaronyl (Fmoc) amino acids (using a fourfold molar excess) in a microwave synthesizer (CEM Discover). The peptide was cleaved using a trifluoroacetic acid (TFA):water:1,2-ethanedithiol ratio of 95:2.5:2.5. Peptide purification was run on a semi reverse phase HPLC (Vydac, C4 column, 250 mm × 10 mm i.d.) at 60 °C in a gradient between solvent A (water with 0.1% TFA) and solvent B′ (isopropanol: acetonitrile:water in a ratio of 6:3:1 with 0.1% TFA). The identity and purity of the peptide were confirmed by MALDI-TOF mass spectrometry (Voyager model DE RP; PerSeptive Biosystems) and analytical reverse phase HPLC (Vydac C4 column).

Sedimentation Equilibrium of Analytical Ultracentrifugation (AUC). Sedimentation equilibrium experiments and data analysis were performed as described previously (1–3). Wild-type and mutant Q120A FPs was mixed with dodecylphosphocholine (DPC) in 2,2,2-trifluoroethanol (TFE). The cocktail was dried in a glass vial, lypholized overnight, and rehydrated with buffer in order to reach the DPC concentration of 8 mM. This pH 7.3 buffer contained 100 mM Hepes, 100 mM NaCl, and 37% D_2O in order to match the density of the detergent.

Three groups of samples were prepared as peptide:DPC molar ratios of 1:50, 1:100, and 1:200. The experiments were conducted at 25 °C using a Beckman XL-I analytical ultracentrifuge at 30, 35, 40, and 45 kRPM. In addition, some samples used additional experiments at 48 kRPM. Data obtained were globally fitted to a nonlinear least-squares curve by IGOR Pro (Wavemetrics) as previously described (4).

Two AUC experiments were carried out to identify the interaction between the FP and the C-term-TM peptide. First, the C-term-TM peptide alone was prepared as a peptide:DPC molar ratio of 1:100. No significant curvature has been observed in AUC data despite running the sample at multiple speeds (30, 35, 40, 45 and 50 kRPM). The C-Term-TM peptide and the FP were mixed in a 1:1 molar ratio at a total peptide:DPC molar ratio of 1:50 (Fig. S3*B*, *Left*) and 1:100 (Fig. S3*B*, *Right*). The buffer conditions and AUC experimental protocol were the same for both the C-term-TM peptide alone and in combination with the FP. The FP used here was synthesized using the original sequence, without Trp labeled, thus the FP itself did not have absorbance at 280 nm. The significant curvature from the mixture suggests the strong interaction between C-term-TM peptide and FP. The concentration of the C-term-TM peptide was identified based on the absorbance at 280 nm. The concentration of the FP was identified using a micro-balance and dissolved in TFE. Thus the determined concentration for the FP here might have 5% error from absorbing water from atmosphere and presumably contributed the fitting error in the left side of the curves.

To estimate a lower limit of the strength of C-term-TM association with FP, the avidity of C-term-TM homooligomerization with and without FP were compared. For C-term-TM alone, the association is weak. Association becomes observable only in the range of 1:3–1:5 peptide:detergent ratio. Association is similar when fit as a dimer, trimer, or hexamer. In the presence of FP, the midpoint of heteromeric association occurs at approximately 1:100 peptide:detergent. Because the heteromeric interaction appears to involve an equal number of FP and C-term-TM peptides, for this calculation the molecular weight, extinction coefficient, and partial specific volume values for the FP and C-term-TM were averaged and fit to a monomer-12mer equilibrium. The ratio of these self-association values provides a conservative estimate of C-term-TM association of at least 20 times stronger association in the presence of FP than in isolation.

Circular Dichroism (CD). CD spectra were collected with a Jasco J-810 spectropolarimeter and a 0.1-cm quartz cell using a 1-nm step at 25 °C. Peptide at 12.5 μM was incorporated into 2.5-mM detergent DPC using the method described above and rehydrated into aqueous buffer containing 10-mM disodium phosphate of pH 7.4. The CD spectrum of each peptide was obtained by subtracting the spectrum of DPC alone and averaging over three scans.

Attenuated Total Reflection IR Spectroscopy (ATR-IR). ATR-IR experiment and data analysis were conducted as previously described (5, 6). 140 μL of 300-μM wild-type or Q120A mutant FP was mixed with 25.5 μL of 32.9-mM 1-palmitoyl-2-oleoyl-sn-glycero-3-phosphocholine (POPC), in order to make a peptide: POPC ratio 1:20. The cocktail was loaded on the surface of ATR Ge crystal evenly and dried by air. The film was rehydrated by D_2O-saturated air overnight in closed environment of D_2O bath. All infrared spectra were measured in a Nicolet Magna-IR 860 spectrometer using 1 cm^{-1} resolution. During data acquisition high-purity N_2 gas continuously purged the spectrometer, and D_2O-hydrated high-purity N_2 gas was continuously purged upon the sample film to eliminate the spectral effects of water in air. The polarized mirror was adjusted to 0° and 90° in order to create incident light oriented parallel and perpendicular to the lipid normal, respectively. Each spectrum of a peptide was subtracted by the spectrum of the crystal alone at 0° and 90°, respectively. A total of 64 scans were averaged and Fourier transformed to both wild type and mutant. The dichroic ratio of 1656 cm^{-1} amide I bond absorption is computed for parallel (0°) versus perpendicular (90°) polarized incident light relative to the membrane normal. The dichroic ratio was then applied to equations in ref. 5 in order to calculate the peptide orientation relative to the membrane normal.

Sequence Conservation. Because buried positions are more conserved than solvent or lipid exposed positions, an α-helix will, in general, show a sinusoidal conservation pattern with approximately 3.6 residue periodicity (7). If the helix is bent as part of a coiled coil, seven residues occur over every two turns of the helix, giving an average of 3.5 residue periodicity. A beta sheet, however, would be expected to show approximately two residues per period, as the residues alternate sides of the strand.

To determine the sequence conservation of the FP, sequences from the National Center for Biotechnology Information nonre-

dundant database (February 9, 2009) were selected if the sequence matched the PIV5 FP sequence (FAGVVIGLAALGVATAAQVTAAVAL) to an E-value of 1 or less (8). The program Cd-hit (9) was used to remove sequences with higher than 90% sequence identity. The sequence entropy of each sequence position is calculated as: Entropy $= -\Sigma_{i=1,20}\{f_i \ln f_i\}$, where f_i is the fraction of residue i. The entropy, x, was fit to a sine wave according to the formula: $y = a * \sin[2\pi(x+b)/c] + d$, where the periodicity is found in variable c.

Creation of Coiled-Coil Models. All-atom protein backbones of the TM coiled-coil FP hexameric bundle (6HB) were created using the Crick parameterization (10) according to a previously published method (11). Three parameters were allowed to vary: alpha helical phase (ϕ), pitch angle (α), and superhelical radius (R). The other coiled-coil parameters were held fixed. The ϕ was varied from 0° to 359° in 1° steps; α from 5° to 20° in 1° steps; and R from 9.0 to 11.0 Å in 0.1 Å steps. These ranges were chosen based on the values observed in other coiled coils (12) and such that no backbone clashes would occur in the complex.

For each backbone 6HB model, side chains were placed using the program scap (13) and hydrogens placed by reduce (14). Each structure was subject to a constrained minimization in CHARMM22 (15) of 50 steps to decrease, but not remove, the penalty for a clash in a given structure and to not move significantly from the initial coiled-coil parameters. The energy of the structure was then calculated using CHARMM22 and IMM1 implicit solvation (16) with a nonbonding interaction cutoff of 9.0 Å. The selected minimized models had the following (ϕ, R, α) parameters before simulation: (40°, 10.3 Å, 22.1°), (43°, 10.4 Å, 15.9°), (88°, 10.4 Å, 16.0°), (196°, 9.7 Å, 13.6°), and (300°, 10.7 Å, 15.6°). The parameters of the antiparallel model were: (24°, 10.2 Å, 9.0°) with a z offset of 0.5 Å.

Molecular Dynamics (MD) Simulations. Models of the FP hexameric bundle (6HB) were embedded in a lipid bilayer composed of 140 POPC molecules (80 × 80 Å in size), capped on each side by a water layer of 18-Å thickness (6,500 water molecules in total). Periodic boundary conditions were applied. Eleven Na^+ and 11 Cl^- ions were distributed in the water region, corresponding to a salt concentration of about 150 mM. The six peptides and the ions were described by the CHARMM27 force field (17), the water molecules by the TIP3P force field (18), and the lipid molecules by the united-atom force field recently developed by Hénin et al., which provides nearly identical physicochemical properties to the CHARMM27 lipid (19). The van der Waals interactions were truncated at 12 Å, and a grid resolution of 0.75 Å was used to treat the electrostatic interactions with the particle-mesh Ewald scheme (20).

Each 6HB system was simulated by MD, using a time step of 2 fs. A Langevin thermostat (21) was applied to maintain a temperature at 310 K (~37 °C), and a Langevin-piston barostat (22) to keep a pressure of 1 bar along the bilayer normal. In the two directions parallel to the membrane, instead, a constant surface tension of 20 dyn/cm^2 was enforced. The NAMD program (23) was used to perform all the MD calculations presented here.

Because the interactions between the peptides and the surrounding lipids are of major importance to this study, and due to the fact that the starting 6HB structures were modeled within an implicit membrane, a rather long equilibration phase was performed. For each starting structure, a restraint of 10 kcal · mol^{-1} · Å^{-1} was applied to the peptide heavy atoms for the first 2 ns and on the backbone heavy atoms only for the following 7 ns. The time evolution of the system was monitored during the following 50 ns of MD simulation without restraints.

The density of water oxygen atoms in Fig. S6 was computed by counting all atoms within a radius of 12 Å from the central axis of the bundle. We used this criterion to account for the wide aperture of certain 6HB models (ϕ = 88°, 300°) and the oscillations of the bundle with respect to the membrane normal, while not including at the same time a detectable number of water molecules in the lipid interstitial regions: Water density profiles computed with different radii do not differ significantly between $z = -15$ and 15 Å. The water density isosurface in Fig. S7 shows instead the distribution of all water molecules of the system in the HB (ϕ = 40°) simulation.

FTIR Dichroism Calculations. Following the method of Arkin and coworkers (24), we calculated the expected dichroism ratio by summing the contributions of carbonyl groups to each polarization given the backbone dipoles vectors in the MD trajectory. For these calculations, 5% disorder was assumed. Because nonhelical termini and the first three helical residues are expected to exchange with D_2O, only residues 108–126 were used for the calculation. Including the full FP gives very similar results.

Modeling the Fusion Process. To model the fusion process, both the PIV5 F protein and the membrane needed to be treated. A 200-Å by 200-Å POPC lipid bilayer was created using VMD (25). For early stages of the fusion model, the bilayer was perturbed using a cosine function with increasing amplitude centered at the region that would become the point of membrane apposition. Later stages incorporated increasing fractions of the conformation of a catenoid that makes up the final, postfusion conformation of the model. The diameter of this pore is estimated to be 20 Å based on experimental results for influenza hemagglutinin (26, 27). For the catenoid, the midpoint of the membrane followed the mathematical formula while lipids were rotated to be perpendicular to the surface. Lipid density was maintained between the initial flat membrane surface and the catenoid structure.

To model the F protein, first the available prefusion and postfusion crystal structures were combined to create a model of the prehairpin intermediate that bridges the viral and target cell membranes. Transmembrane domains were modeled either as coiled coils extended into the membrane or using the existing model of the prefusion TM (28). Loops were modeled using loopy (29), the side chains were repacked using Rosetta (30), and the structure minimized using the CHARMM22 energy function (15). The structure of the postfusion state comes from the closely related hPIV3; the sequence of PIV5 was threaded onto the structure using Rosetta and minimized using the CHARMM energy function.

For fusion intermediates, the membrane associated domains were first modeled. The hexameric model of the fusion protein was taken as the initial state for the prehairpin intermediate. The helices were then tilted in 10° increments and slowly moved outward from the center to mimic the conformational change proposed for the MscL channel (31). In parallel, two TM domain trimers (28) were initially at a distance due to the conformation of the prehairpin intermediate, then brought close together and tilted relative to each other as may occur under the tension caused by zippering of the soluble coiled-coil domains.

The soluble portions of the F protein trimers were tilted to connect to the FPs at each step. Loops between the FP and heptad repeat A were connected using loopy (29) and Pymol sculpting. The conformation of the exterior coiled coil, heptad repeat B, was then modified to connect to the TM domain using an in-house loop modeling program and the BBQ backbone modeling program (32).

1. Zhang Y, Kulp DW, Lear JD, DeGrado WF (2009) Experimental and computational evaluation of forces directing the association of transmembrane helices. *J Am Chem Soc* 131:11341–11343.
2. Yin H, et al. (2007) Computational design of peptides that target transmembrane helices. *Science* 315:1817–1822.
3. Cristian L, Lear JD, DeGrado WF (2003) Determination of membrane protein stability via thermodynamic coupling of folding to thiol-disulfide interchange. *Protein Sci* 12:1732–1740.
4. Kochendoerfer GG, et al. (1999) Total chemical synthesis of the integral membrane protein influenza A virus M2: role of its C-terminal domain in tetramer assembly. *Biochemistry* 38:11905–11913.
5. Menikh A, Saleh MT, Gariepy J, Boggs JM (1997) Orientation in lipid bilayers of a synthetic peptide representing the C-terminus of the A1 domain of shiga toxin. A polarized ATR-FTIR study. *Biochemistry* 36:15865–15872.
6. Tucker MJ, Getahun Z, Nanda V, DeGrado WF, Gai F (2004) A new method for determining the local environment and orientation of individual side chains of membrane-binding peptides. *J Am Chem Soc* 126:5078–5079.
7. Komiya H, Yeates TO, Rees DC, Allen JP, Feher G (1988) Structure of the reaction center from Rhodobacter sphaeroides R-26 and 2.4.1: symmetry relations and sequence comparisons between different species. *Proc Natl Acad Sci USA* 85:9012–9016.
8. Altschul SF, Gish W, Miller W, Myers EW, Lipman DJ (1990) Basic local alignment search tool. *J Mol Biol* 215:403–410.
9. Li W, Godzik A (2006) Cd-hit: A fast program for clustering and comparing large sets of protein or nucleotide sequences. *Bioinformatics* 22:1658–1659.
10. Crick FHC (1953) The Fourier transform of a coiled-coil. *Acta Crystallogr* 6:685–689.
11. North B, Summa CM, Ghirlanda G, DeGrado WF (2001) D(n)-symmetrical tertiary templates for the design of tubular proteins. *J Mol Biol* 311:1081–1090.
12. Grigoryan G, DeGrado WF (2011) Probing designability via a generalized model of helical bundle geometry. *J Mol Biol* 405:1079–1100.
13. Xiang Z, Honig B (2001) Extending the accuracy limits of prediction for side-chain conformations. *J Mol Biol* 311:421–430.
14. Word JM, Lovell SC, Richardson JS, Richardson DC (1999) Asparagine and glutamine: using hydrogen atom contacts in the choice of side-chain amide orientation. *J Mol Biol* 285:1735–1747.
15. MacKerell AD, Jr, et al. (1998) All-atom empirical potential for molecular modeling and dynamics studies of proteins. *J Phys Chem B* 102:3586–3616.
16. Lazaridis T (2003) Effective energy function for proteins in lipid membranes. *Proteins* 52:176–192.
17. MacKerell AD, Jr, Banavali N (2000) All-atom empirical force field for nucleic acids: I. Parameter optimization based on small molecule and condensed phase macromolecular target data. *J Comput Chem* 21:86–104.
18. Jorgensen WL, Chandrasekhar J, Madura JD, Impey RW, Klein ML (1983) Comparison of simple potential functions for simulating liquid water. *J Chem Phys* 79:926–935.
19. Hénin J, Shinoda W, Klein ML (2008) United-atom acyl chains for CHARMM phospholipids. *J Phys Chem B* 112:7008–7015.
20. Essman U, et al. (1995) A smooth particle mesh Ewald method. *J Chem Phys* 103:8577–8593.
21. Adelman SA, Doll JD (1976) Generalized Langevin equation approach for atom/solid-surface scattering—General formulation for classical scattering off harmonic solids. *J Chem Phys* 64:2375–2388.
22. Martyna GJ, Tobias DJ, Klein ML (1994) Constant-pressure molecular-dynamics algorithms. *J Chem Phys* 101:4177–4189.
23. Phillips JC, et al. (2005) Scalable molecular dynamics with NAMD. *J Comput Chem* 26:1781–1802.
24. Manor J, et al. (2009) Gating mechanism of the influenza A M2 channel revealed by 1D and 2D IR spectroscopies. *Structure* 17:247–254.
25. Humphrey W, Dalke A, Schulten K (1996) VMD: Visual molecular dynamics. *J Mol Graphics* 14:33–38, 27–38.
26. Spruce AE, Iwata A, Almers W (1991) The first milliseconds of the pore formed by a fusogenic viral envelope protein during membrane fusion. *Proc Natl Acad Sci USA* 88:3623–3627.
27. Bonnafous P, Stegmann T (2000) Membrane perturbation and fusion pore formation in influenza hemagglutinin-mediated membrane fusion. A new model for fusion. *J Biol Chem* 275:6160–6166.
28. Bissonnette ML, Donald JE, DeGrado WF, Jardetzky TS, Lamb RA (2009) Functional analysis of the transmembrane domain in paramyxovirus F protein-mediated membrane fusion. *J Mol Biol* 386:14–36.
29. Soto CS, Fasnacht M, Zhu J, Forrest L, Honig B (2008) Loop modeling: Sampling, filtering, and scoring. *Proteins* 70:834–843.
30. Kuhlman B, et al. (2003) Design of a novel globular protein fold with atomic-level accuracy. *Science* 302:1364–1368.
31. Liu Z, Gandhi CS, Rees DC (2009) Structure of a tetrameric MscL in an expanded intermediate state. *Nature* 461:120–124.
32. Gront D, Kmiecik S, Kolinski A (2007) Backbone building from quadrilaterals: A fast and accurate algorithm for protein backbone reconstruction from alpha carbon coordinates. *J Comput Chem* 28:1593–1597.

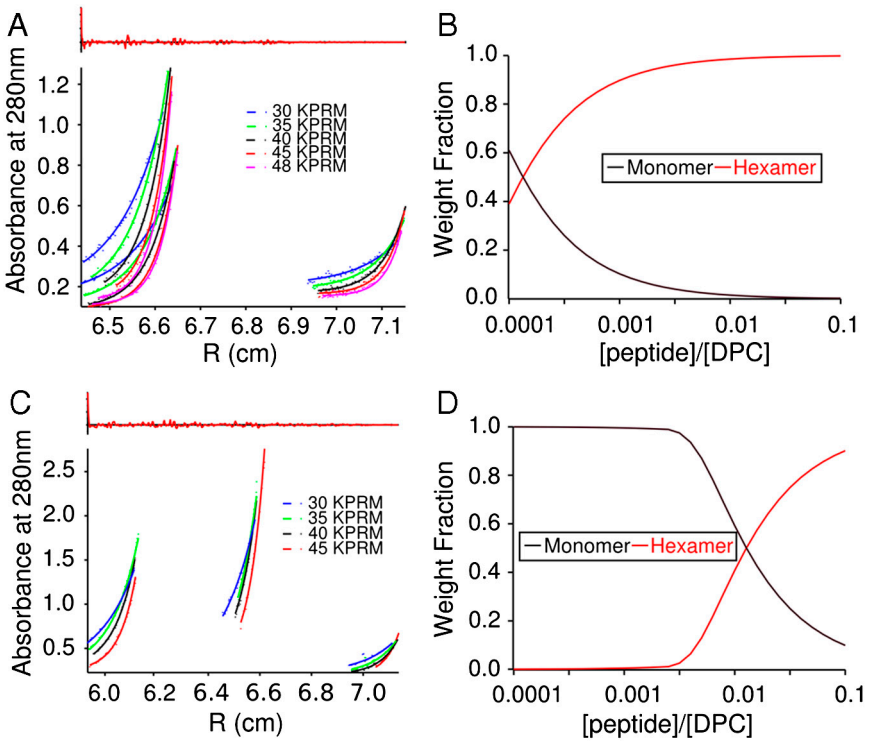

Fig. S1. AUC of FP wild-type (*A*, *B*) and mutant Q120A (*C*, *D*). Single species fitting of wild-type (*A*) and mutant Q120A (*C*) PIV5 FP suggests both associate as hexamers. The *Top* of each panel shows the residuals of single species fitting. The species weight fraction is shown for wild-type (*B*) and mutant Q120A (*D*), indicating that hexamer is the dominant species composition for the wild type, while oligomerization of the mutant Q120A requires significantly higher mole fractions.

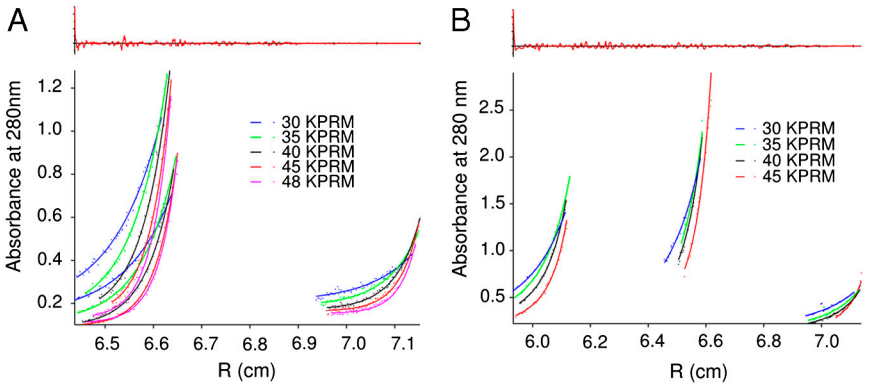

Fig. S2. Sedimentation equilibrium analysis of the wild-type (*A*) and mutant Q120A (*B*) FPs in DPC micelles. The absorbance was measured at 280 nm. The data was fitted as a monomer–hexamer equilibrium, resulting in a $pK_{dissociation}$ of 20.1 for the wild-type and a $pK_{dissociation}$ of 10.2 for the mutant Q120A. The *Top* of each panel shows the residuals of the fit. In this data analysis, the concentration of peptide is the mole ratio of peptide/detergent and therefore is unitless.

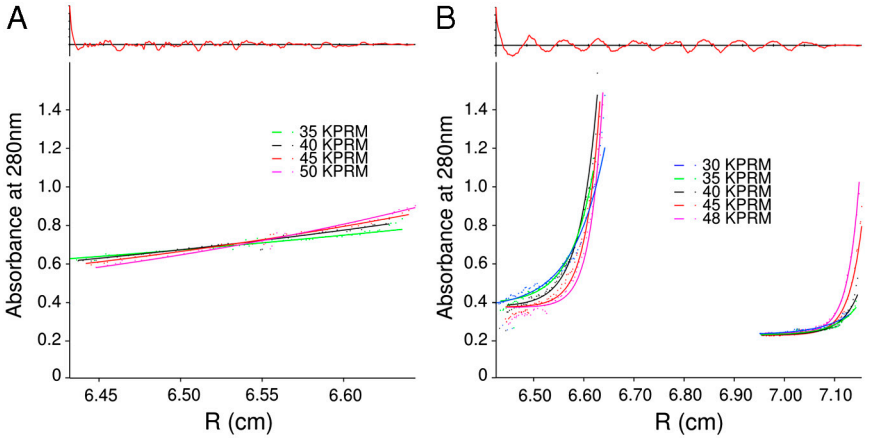

Fig. S3. AUC of C-term-TM peptide alone (*A*) and C-term-TM peptide–FP mixture (*B*). No significant curvature has been observed in AUC data of TM peptide alone (*A*), suggesting that C-term-TM peptide does not self-associate under these conditions. Single species fitting for a 1:1 mixture of C-term-TM peptide and FP (using the original sequence without a Trp label) suggests a strong interaction between these peptides.

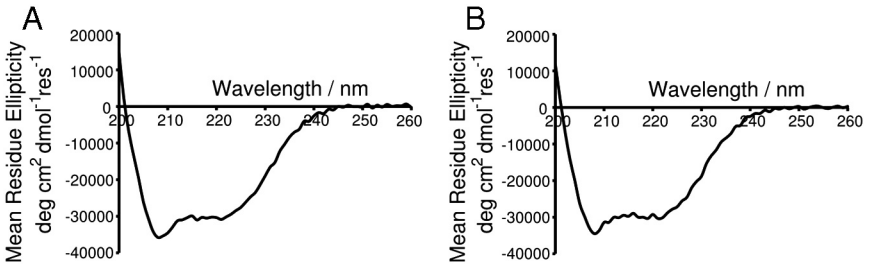

Fig. S4. CD spectra of FP wild-type (*A*) and mutant Q120A (*B*). The spectra show that both wild-type and Q120A are predominantly α-helical at a peptide:DPC ratio of 1:200.

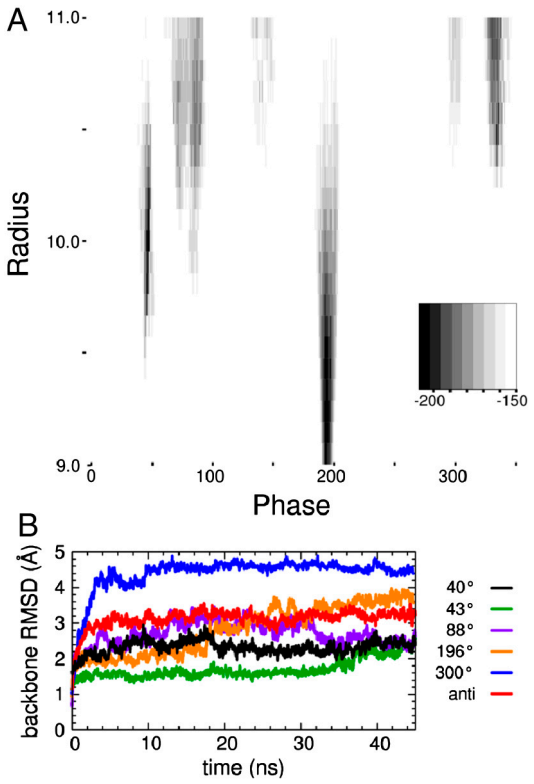

Fig. S5. Computational prediction of the hexameric helical bundle. (*A*) Heat map shows predicted energies of coiled-coil models with different radii and phases. Regions in black are predicted to be more energetically favorable. (*B*) Backbone atom rmsd of five coiled-coil models selected from *A* and one antiparallel model generated using an analogous procedure. Parallel models are labeled according to their phase angle.

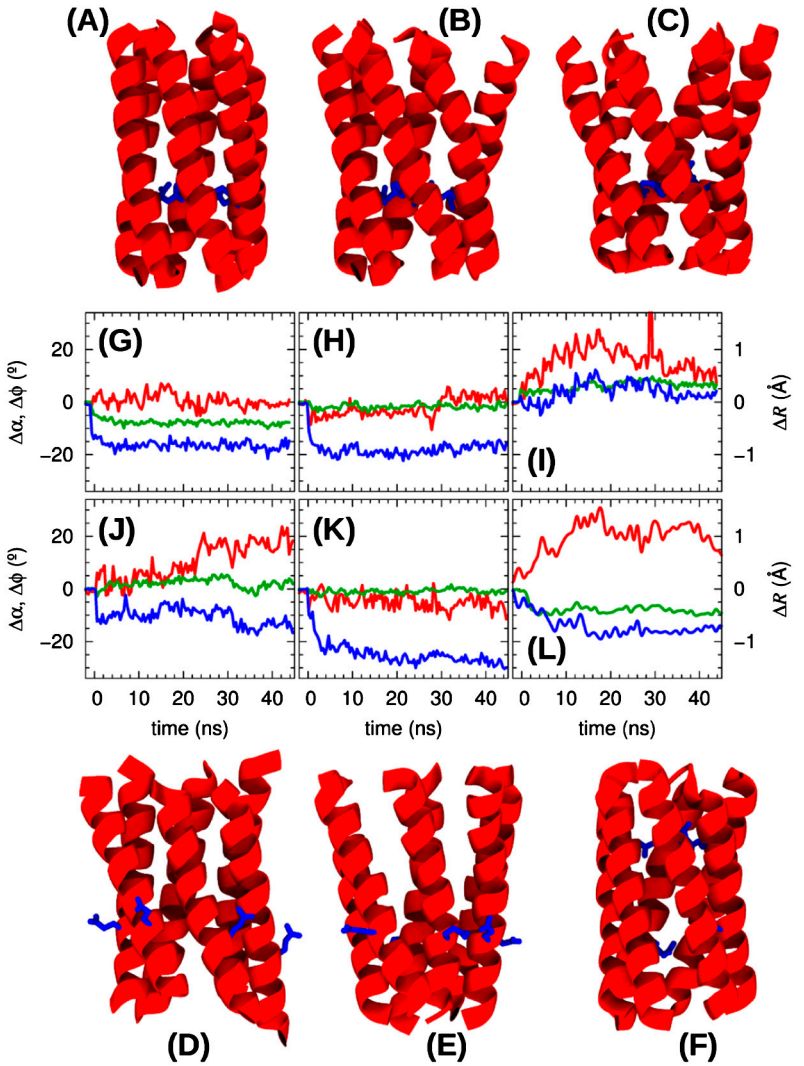

Fig. S6. Final structures of the MD simulations of different hexamer models and coiled-coil parameters as a function of time. (*A–F*) Final backbone structures in cartoon representations of five parallel models of the hexamers corresponding to the phase angles, ϕ, of 40° (*A*), 43° (*B*), 88° (*C*), 192° (*D*), 300° (*E*), and of the antiparallel model (*F*). The heavy atoms of the Gln120 side chains are drawn in blue. (*G–L*) Coiled-coil parameters as a function of time of the six models, in the same order as in (*A–F*); the deviations from the initial values of the pitch angle α and of the phase angle ϕ ($\Delta\alpha$ and $\Delta\phi$) are plotted in green and red, respectively; the deviation of the radius (Δr) is plotted in blue.

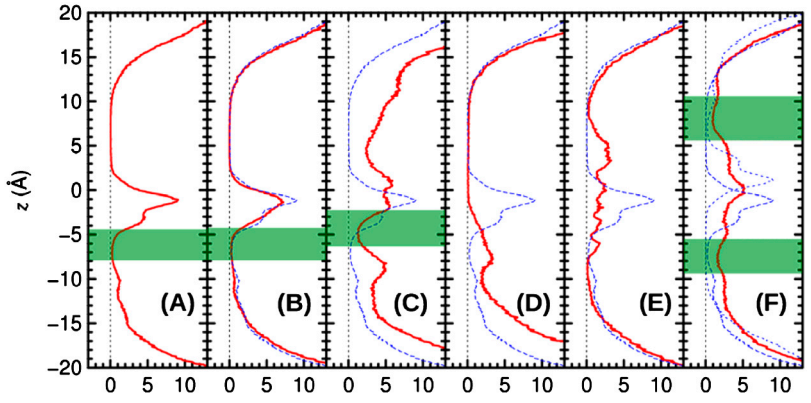

Fig. S7. Density of oxygen atoms from water molecules through the pore of the hexamer bundle. From *Left* to *Right*, data from the following models are plotted: $\phi = 40°$, 43°, 88°, 192°, 300°, and the antiparallel model. The density is expressed in number of atoms per angstrom and plotted as a red line along the horizontal axis. For comparison, the density profile from the $\phi = 40°$ model is also shown as a dashed blue line in the other models (duplicated for the antiparallel model, which is symmetric with respect to the membrane plane). For those models featuring pore-lining Gln120 side chains, the region occupied by their nitrogen and oxygen atoms is highlighted in green.

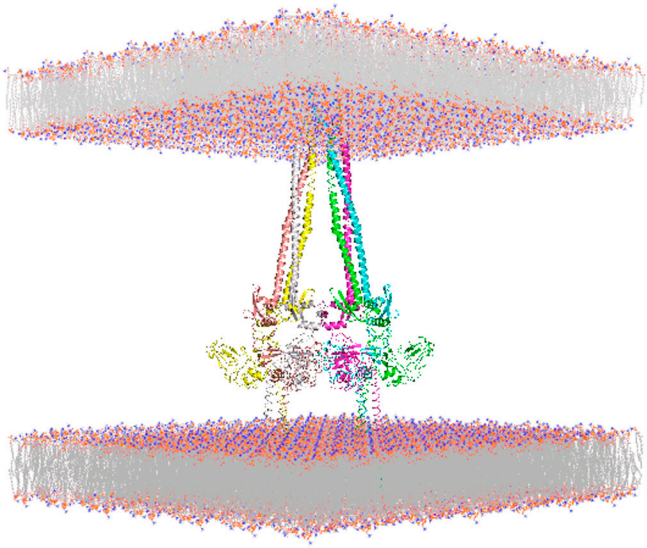

Movie S1. How a hexamer of the PIV5 FPs might serve as a pinprick to nucleate a fusion pore. As the conformational change progresses, the TM bundles formed by the C-term-TM and FP helices first dock, then coalesce into heteromeric bundles. The initial zone of intermembrane contact involves favorable protein–protein interactions rather than energetically unfavorable dehydration of the bilayer headgroups, and the fusion of these two helical bundles provides a low-energy pathway to direct fusion of the bilayers, which remain associated with the TM bundles throughout the process.

Movie S1 (GIF)

Table S1. Conservation of small residues (Ala, Gly) within four virus families

Orthomyxoviridae:	
Influenza A H1	GLFGAIAGFIEGGWTGMIDGWYG
Influenza A H3	GLFGAIAGFIENGWEGMIDGWYG
Influenza A H5	GLFGAIAGFIEGGWQGMVDGWYG
Influenza B	GFFGAIAGFLEGGWEGMIAGWHG
Influenza C	IFGIDDLIIGVLFVAIVETGIGGYLLGS
Retroviridae:	
HIV-1, group M, clade A	AIGMGAFFLGFLGAAGSTMGAASITLTVQA
HIV-1, group M, clade B	AVGIGALFLGFLGAAGSTMGAASMTLTVQA
HIV-1, group M, clade C	AVGIGAVFLGFLGAAGSTMGAASITLTVQV
HIV-1, group O	AVGLGMLFLGVLSAAGSTMGAAATTLAVQT
HIV-1, group N	AAFGLGALFLGFLGAAGSTMGAASITLTVQA
HIV-2	GVFVLGFLGFLATAGSAMGAASLTLSAQS
SIV, rhesus monkey	GVFVLGFLGFLATAGSAMGAASLTLTAQS
SIV, chimpanzee	AAFGLGALFLGFLGAAGSTMGAAAVTLTVQA
Human T-cell leukemia virus	AVPVAVWLVSALAMGAGVAGGITGSMSLASG
Paramyxoviridae:	
Human parainfluenza virus 1	FFGAVIGTIALGVATAAQITAGIALA
Human parainfluenza virus 3	FFGGVIGTIALGVATSAQITAAVALV
Simian parainfluenza virus 5	FAGVVIGLAALGVATAAQVTAAVALV
Measles	FAGVVLAGAALGVATAAQITAGIAL
Sendai virus	FFGAVIGTIALGVATSAQITAGIALA
Nipah virus	LAGVIMAGVAIGIATAAQITAGVALY
Newcastle virus	FIGAIIGSVALGVATAAQITAASALI
Respiratory syncytial virus	FLGFLLGVGSAIASGVAVS
Arenaviridae:	
Lassa fever	GTFTWTLSDSEGKDTPGGYCLT
Lymphocytic choriomeningitis	GTFTWTLSDSSGVENPGGYCLT
Junin arenavirus	AFFSWSLTDSSGKDTPGGYCL
Machupo virus	AFFSWSLTDSSGKDMPGGYCL
Guanarito virus	AFFSWSLSDPKGNDMPGGYCL
Sabia virus	GIFSWTITDAVGNDMPGGYCL

Each family uses a type I fusion protein with an N-terminal FP. Small residues are shown in bold. Note that even distantly related viruses often conserve the position of small residues.